An integrated cleanroom process for the vapor phase deposition of large-area zeolitic imidazolate framework thin films

Alexander John Cruz, Ivo Stassen, Mikhail Krishtab, Kristof Marcoen, Timothée Stassin, Sabina Rodriguez-Hermida, Joan Teyssandier, Sven Pletincx, Johan Meersschaut, Philippe Vereecken, Víctor Rubio-Giménez, Sergio Tatay, Carlos Martí-Gastaldo, Steven de Feyter, Tom Hauffman, and Rob Ameloot*

A. J. Cruz, I. Stassen, M. Krishtab, T. Stassin, S. Rodriguez-Hermida, P. Vereecken, R. Ameloot

Centre for Membrane Separations, Adsorption, Catalysis, and Spectroscopy for Sustainable Solutions, Department of Microbial and Molecular Systems, KU Leuven - University of Leuven, Celestijnenlaan 200F, 3001 Leuven, Belgium

E-mail: rob.ameloot@kuleuven.be

A. J. Cruz, K. Marcoen, S. Pletincx, T. Hauffman

Research Group of Electrochemical and Surface Engineering, Department of Materials and Chemistry, Vrije Universiteit Brussel, Pleinlaan 2, 1050 Brussels, Belgium

A. J. Cruz, I. Stassen, M. Krishtab, K. Marcoen, J. Meersschaut, P. Vereecken

imec, Kapeldreef 75, 3001 Leuven, Belgium

J. Teyssandier, S. De Feyter

Division of Molecular Imaging and Photonics, Department of Chemistry, KU Leuven - University of Leuven, Celestijnenlaan 200F, 3001 Leuven, Belgium

V. Rubio-Gimenez, S. Tatay, C. Martí-Gastaldo

Instituto de Ciencia Molecular, Universitat de València, Catedrático José Beltrán 2, 46980 Paterna, Spain

I. Stassen

(present address) Department of Chemistry, Massachusetts Institute of Technology, 77 Massachusetts Avenue, Cambridge, Massachusetts 02139, United States

Robust and scalable thin film deposition methods are key to realize the potential of metal-organic frameworks (MOFs) in electronic devices. Here, we report the first integration of the chemical vapor deposition (CVD) of MOF coatings in a custom reactor within a cleanroom setting. As a test case, the MOF-CVD conditions for ZIF-8 are optimized to enable smooth, pinhole-free, and uniform thin films on full 200 mm wafers under mild conditions. The single-chamber MOF-CVD process and the impact of the deposition parameters are elucidated *via* a combination of *in situ* monitoring and *ex situ* characterization. The resulting process guidelines will pave the way for new MOF-CVD formulations and a plethora of MOF-based devices.

Apart from their applications in catalysis[1], gas storage[2], and separation processes[3], metal-organic frameworks (MOFs), with their unprecedented specific surface area and chemical modularity, show tremendous potential for integration in microelectronics[4,5]. As sensor coatings, their tunable composition and crystalline structure can be exploited for the selective adsorption of target molecules[6–8]. The low dielectric constant resulting from their porosity makes MOFs prime candidates for high-performance insulators in future logic processors[9]. To capitalize on the properties of MOFs in these areas, the development of a robust method to deposit thin and defect-free coatings is vital. This challenge has been a bottleneck for all microporous and crystalline materials tested in the context of electronic devices, as traditional wet synthesis procedures are incompatible with fabrication requirements due to contamination, corrosion, and limited control over the deposition process[4,10–12].

Although crystalline coordination polymers have been deposited from gaseous precursors, the resulting materials have no measurable porosity[13–15]. Most attempts to deposit MOFs *via* all-vapor phase processes yielded non-porous or non-crystalline films unless subjected to post-deposition treatments such as crystallization in a reactive atmosphere[16–20]. While these studies are valuable in providing insight into the chemistry needed to form MOFs on surfaces, an integrated process that can be extended to large-area substrates is necessary. We previously reported the chemical vapor deposition (CVD) of MOF thin films that are crystalline as-deposited, and porous after mild activation[10]. This MOF-CVD process (**Fig. 1**) starts with the deposition of a metal oxide layer, for instance through atomic layer deposition (ALD), by alternating self-limiting surface reactions of volatile reactants (*e.g.*, diethylzinc and water)[21]. When the oxide coating is exposed to a vaporized linker under the right conditions, it undergoes a vapor-solid reaction to yield the desired MOF. As an example, ZIF-8, consisting of Zn(II) and 2-methylimidazolate (mIM)[22], can be formed by exposing a ZnO precursor to a vapor of the protonated linker, HmIM. This method has been adopted to prepare gas separation membranes, sensors, and energy storage devices[23–26]. In these approaches, tools commonly available in the wet chemistry lab (*i.e.,* glassware and autoclaves) were used to

perform the oxide-to-MOF conversion step. To become accessible to researchers from other fields and thus realize applications that cross subject boundaries, especially in microelectronics, the MOF-CVD process has to be implemented as a cleanroom unit operation and validated using the analysis tools common in such a setting.

In this work, we realize both goals by developing an integrated MOF-CVD reactor and formulating a robust deposition protocol for ZIF-8 as a test case (**Supplementary Fig. 1**). By making use of *in situ* ellipsometry together with complementary *ex situ* characterization techniques, the MOF-CVD mechanism is elucidated and critical deposition parameters are identified. The optimized deposition conditions are translated to full 200 mm wafer substrates, and the uniformity and the absence of pinholes are verified for the resulting coatings.

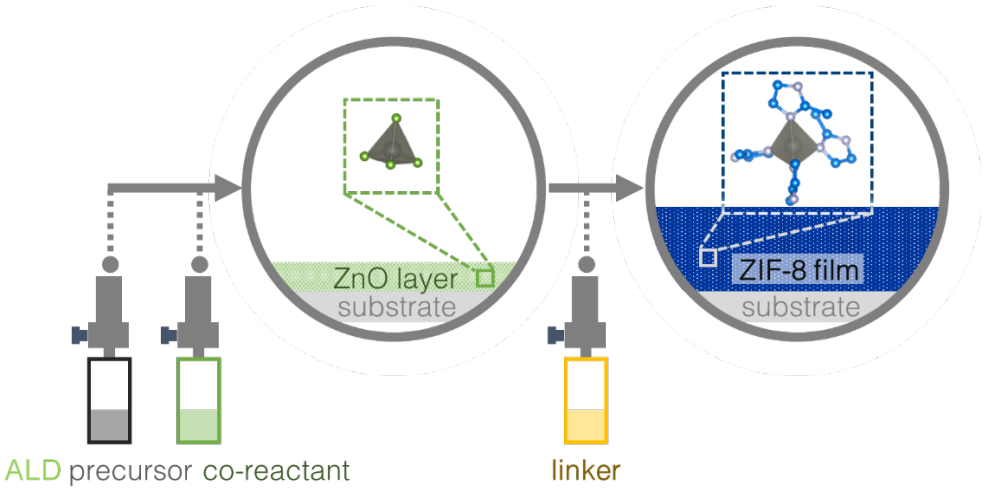

Figure 1 | MOF-CVD process. Step 1) ALD of the metal oxide precursor: $Zn(C_2H_5)_{2\,(g)} + H_2O_{\,(g)} \rightarrow ZnO_{\,(s)} + 2\,C_2H_{6\,(g)}$, followed by Step 2) exposure to the vaporized organic linker initiates the vapor-solid reaction: $ZnO_{\,(s)} + 2\,HmIM_{\,(g)} \rightarrow H_2O_{\,(g)} + ZIF\text{-}8_{\,(s)}$.

Stages in the ZIF-8 MOF-CVD process

Due to the low vapor pressure of HmIM (530 Pa at 125 ºC[27]), this linker was supplied by flowing N_2 through a heated bubbler-type sublimation vessel (**Supplementary Fig. 2,** see *Methods*). Other types of vapor sources for HmIM did not yield crystalline films, including a direct-vapor draw ALD bottle and a heated canister connected to an accumulator. When filling the sublimation vessel, the fresh HmIM powder is first heated and flushed with dry N_2 (100 ºC for 30 min) to remove adsorbed moisture in the powder bed. A typical MOF-CVD run for ZIF-8 consists of first depositing a 3 nm ALD ZnO film, directly followed by exposure to HmIM vapor in the same reaction chamber, under stopped-flow conditions. The cylindrical cross-flow MOF-CVD reactor chamber is 5 mm-high, can hold substrates up to 200 mm in diameter, and is equipped with independently controlled heating zones. The conversion of the ZnO film into a ZIF-8 layer is achieved only when a temperature gradient is applied between the reactor wall (150 ºC) and the substrate, as further confirmed in a different reactor setup (**Supplementary Fig. 3-4**). This condition is analogous to polymer-CVD[28,29] and likely associated with HmIM adsorption on the ZnO surface (**Supplementary Fig. 5**). The applied thermal gradient must strike a balance between the rate of oxide-to-MOF conversion and linker adsorption. In this reactor configuration and for a fixed reactor wall temperature, a substrate temperature of 80 ºC was found to be optimal.

Due to the organic linker and porosity in the ZIF-8 crystal lattice, a pronounced thickness increase is expected when the MOF is formed from the dense ZnO layer. Time-resolved *in situ* ellipsometry data shows a sigmoidal thickness expansion of the oxide precursor as a function of HmIM exposure time (**Fig. 2a, Supplementary Fig. 6**). A similar profile has been observed in *in situ* powder XRD, for the crystalline ZIF-8 content as a function of time during the solvent-free reaction of HmIM and ZnO[10]. From this MOF-CVD growth curve, three stages can be distinguished. Immediately after the introduction of HmIM, a limited thickness increase is observed (Stage A). Briefly after, a monotonic S-shaped rise in thickness is recorded (Stage

B) followed by the formation of a continuous, 31 nm-thick ZIF-8 film (Stage C). Quartz crystal microbalance (QCM) monitoring of the ZIF-8 MOF-CVD process displays a similar sigmoidal profile as a function of HmIM exposure time (**Supplementary Fig. 7**). The temporal mismatch of the mass gain and ellipsometry thickness evolution is likely due to the different heater configuration employed with the QCM setup and the limitations of the technique in CVD[30,31] (**Supplementary Fig. 8**). The precursor-to-MOF thickness expansion was found to be 10×, lower than the 16-17× expected for crystalline ZnO (hexagonal wurtzite). This difference can be attributed to the low density, defect-rich ALD oxide deposited at 80 ºC[32,33]. In order to quantitatively verify this hypothesis, several techniques were combined. Time-of-flight elastic recoil detection analysis (ToF-ERDA) reveals the presence of excess O in the layer, as would be expected for the presence of hydroxyl defects (**Supplementary Fig. 9**). Rutherford backscattering and X-ray reflectivity measurements yielded a Zn density of $2.75 \pm 0.03 \times 10^{22}$ atoms·cm^{-3} and a film density of 3.9 g·cm^{-3}. These values correspond respectively to 70 % and 66 % of what would be expected for ideal, single-crystal ZnO[34], and therefore explain the lower-than-expected thickness increase. X-ray photoelectron spectroscopy (XPS) confirmed that the low-temperature ALD ZnO has more Zn-OH defects compared to a nanopowder sample (**Supplementary Fig. 10**). These hydroxyl defects are advantageous for the solid-vapor reaction, as they increase the reactivity of the oxide precursor with the linker[10,35].

To collect *ex situ* snapshots, the MOF-CVD process was stopped at selected time points by closing off the HmIM supply line and evacuating the reactor, thereby removing most of the physisorbed species as shown by ellipsometry data (*vide infra*). AFM (**Fig. 2a**) reveals a flat and featureless surface in Stage A, with a root-mean-square roughness (R_{RMS}) of 0.3 nm. The dispersed crystals that appear in Stage B eventually form a pinhole-free ZIF-8 film (Stage C) with exceptional smoothness compared to typical MOF films (R_{RMS} = 4.4 nm)[9,10,23]. Fourier-transform infrared spectroscopy in attenuated total reflection geometry (ATR-FTIR, **Fig. 2b**) reveals that the vibrational fingerprint of ZIF-8 is present in all stages, with growing intensity as a function of HmIM exposure time. This observation suggests that the coordination of Zn^{2+}

to mIM, and thus the reaction of ZnO with HmIM, starts soon after the linker vapor is introduced and is further incorporated in the layer throughout the CVD process. Nevertheless, synchrotron GI-XRD (**Fig. 2c**, **Supplementary Fig. 11**) shows that crystallinity is only detected from Stage B onwards, simultaneously with the observation of crystallite nucleation in AFM.

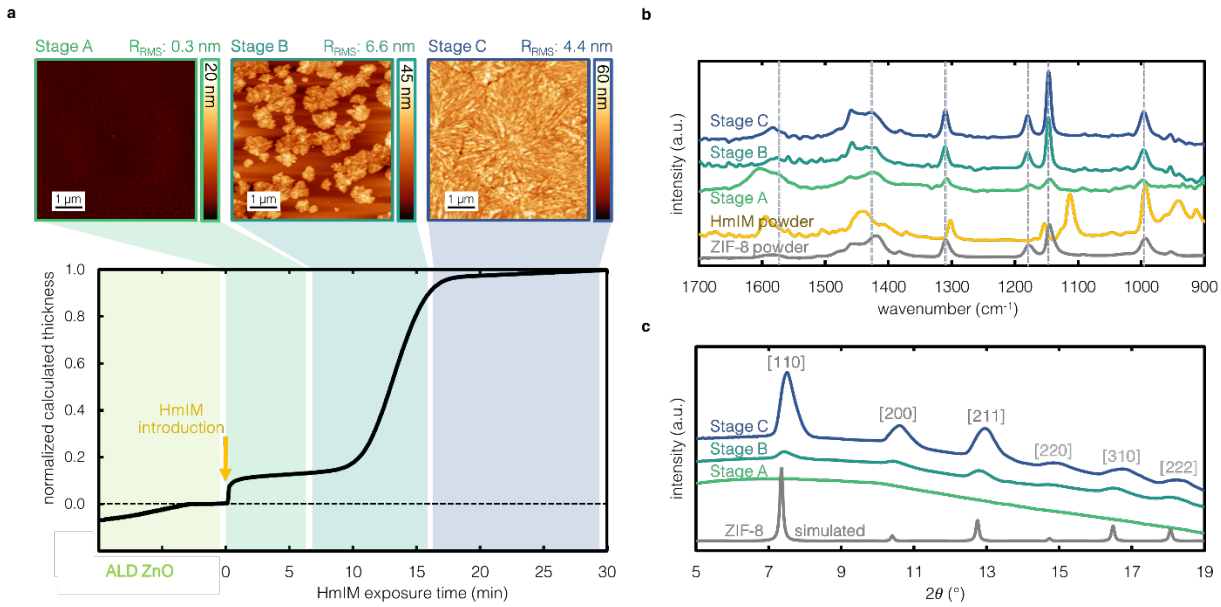

Figure 2 | Monitoring ZIF-8 MOF-CVD. a, Time-resolved *in situ* ellipsometry data and corresponding AFM snapshots of the different growth stages. The surface roughness (R_{RMS}) is calculated for a 6 × 6 µm^2 probe area. Before HmIM is introduced at t = 0 min (yellow arrow), 3 nm of ALD ZnO is deposited on the Si substrate. **b,** Non-normalized ATR-FTIR spectra; commercial ZIF-8 (Basolite Z1200) and HmIM powders are included for reference. **c,** Synchrotron GI-XRD and simulated ZIF-8 diffraction patterns (CCDC code for ZIF-8: VELVOY).

Insights in the ZnO-to-ZIF-8 transformation

XPS confirms that the MOF-CVD ZIF-8 coating exhibits the N 1s signal characteristic of the linker, together with oxygen-containing groups on the top surface of the film (**Supplementary Fig. 12**). To further understand the underlying chemistry and to validate the proposed mechanism for the precursor-to-MOF conversion (**Fig. 3a**), samples were analyzed at each growth stage by time-of-flight secondary ion mass spectrometry (ToF-SIMS). Depth profiling was performed by alternating sputtering and analysis beams. The incorporation of mIM was probed as a function of film depth by measuring C_4N_2-containing ion fragments ($C_4H_6N_2^+$, $C_4H_5N_2^+$, and $C_4H_7N_2^+$, **Fig. 3b**, **Supplementary Section III**). The Stage A film only contains linker near the surface with unreacted ZnO precursor layer underneath. In Stage B, a more pronounced mIM signal extends deeper into the film. The content of Zn-mIM fragments ($ZnC_4H_7N_2^+$) increases similarly as the oxide-to-MOF conversion progresses (**Supplementary Fig. 14**). These observations, together with the data summarized in **Fig. 2**, support the idea of a propagating reaction front during MOF-CVD[10,35] and that a critical linker concentration must be incorporated in the oxide precursor to trigger nucleation. In Stage C, a constant mIM signal is recorded throughout the film thickness, as expected for a ZIF-8 layer.

The reactive incorporation of the mIM linker already early on in the MOF-CVD process is also evident from other observations. When the process is halted by evacuating the reactor in growth Stage A, the thickness decreases only partially and does not fully revert to the ZnO precursor thickness (**Fig. 3c**). In comparison, rapid and complete HmIM desorption is observed when the same procedure is repeated for bare Si substrates. In addition, partially converted samples removed in Stage B, after nucleation has taken place, show an increase in crystal surface coverage from 43 % to 89 % after storage on a lab bench for 30 days (**Supplementary Fig. 15**). This observation suggests that the linker reactively incorporated in the oxide precursor layer can give rise to further crystallization, albeit slowly, even at ambient conditions.

In growth Stage C, HmIM molecules both fill the pores and are adsorbed on the surface of the MOF film. Upon reactor evacuation, the weaker physisorbed molecules on the film surface are removed (**Fig. 3d**). To remove the HmIM adsorbed in the pores, the film was heated to 150 ºC (15 min) under vacuum in the reactor chamber, yielding a final refractive index of 1.33 (λ = 633 nm), in agreement with previous reports[9,36]. Activated and non-activated samples display different relative intensities for the [110] and [200] diffraction lines (**Fig. 3e**), correlated with HmIM pore filling[37–39]. To determine the porosity of the MOF-CVD coatings, Krypton physisorption isotherms were measured for ZIF-8 deposited on high-aspect-ratio micropillar arrays that have a surface area 26× higher compared to flat substrates (**Fig. 3f, Supplementary Fig. 16**). The Brunauer-Emmett-Teller (BET) specific surface area of the MOF-CVD ZIF-8 film, was found to be 35 m^2 per m^2 of (enhanced) substrate area. This sorption data corresponds to an average film thickness of 27 nm, based on the calculated Kr BET surface area for ZIF-8[10,40] (**Supplementary Section IV**). The good agreement between this value and the experimental thickness obtained from ellipsometry (31 nm) indicates that the conformal MOF-CVD ZIF-8 coatings are of high quality. In addition, MeOH isotherms measured for the films *via* ellipsometric porosimetry show an identical adsorption behavior as reported previously for ZIF-8[9,41] (**Supplementary Fig. 17**).

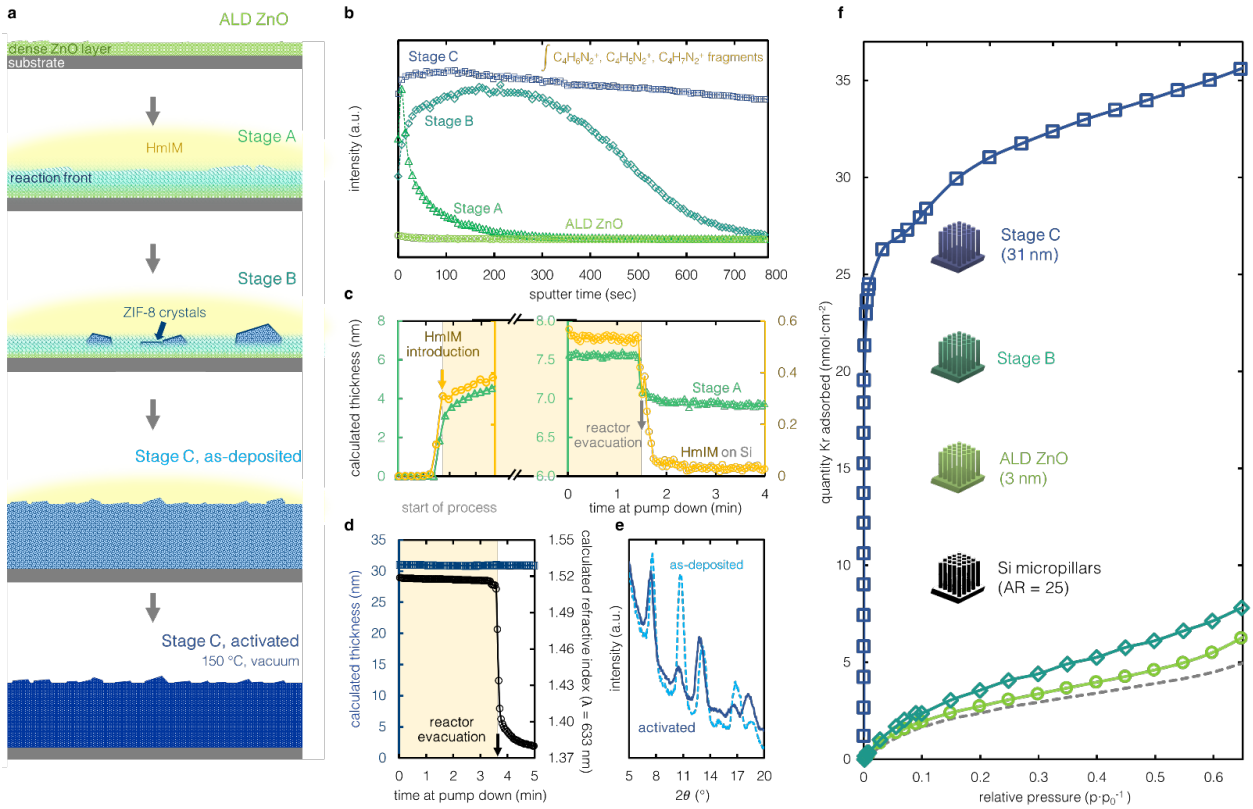

Figure 3 | Insights in the ZnO-to-ZIF-8 transformation. a, Schematic representation of the MOF-CVD growth stages. **b,** ToF-SIMS depth profiles of mIM incorporated in the film at each growth stage. *In situ* ellipsometry profiles for **c,** HmIM desorption after reactor evacuation for the Stage A film with a control experiment on bare Si, and **d,** calculated thickness and refractive index profile during chamber evacuation at the end of the ZIF-8 MOF-CVD process. **e,** GI-XRD patterns of the as-deposited ZIF-8 film (dashed light blue) and the same sample after activation (solid dark blue). **f,** Kr physisorption isotherms for the films deposited on Si micropillars with an aspect ratio of 25. Stage C ZIF-8 (blue squares), Stage B (non-activated, dark green diamonds), ALD ZnO (light green circles) and uncoated substrate (dashed gray).

The role of humidity and oxide precursor thickness

Prior *in situ* powder XRD experiments revealed a faster ZnO-to-ZIF-8 conversion in a humid environment[10]. To test if this behavior holds for thin films, MOF-CVD was performed at a relative humidity of ~12 %. *In situ* ellipsometry data shows a substantial decrease in the time between HmIM introduction and ZIF-8 nucleation (**Fig. 4a, Supplementary Fig. 6, 18**), resulting in a rougher film when compared to the standard, non-humidified deposition conditions (**Fig. 4b, Supplementary Table 2**). Similar to the standard deposition conditions, an amorphous intermediate is formed that exhibits the IR vibrational bands characteristic of ZIF-8. Crystallinity is observed when crystal facets become observable by AFM (**Supplementary Fig. 19**).

Kinetic crystallization models by Avrami[42–44] and Gualtieri[45], previously applied to MOF growth in solution[46–50], were employed to assess the impact of humidification (**Supplementary Section VI**). These methods have also been used to describe the crystallization of thin films based on *in situ* ellipsometry[51,52]. The exponent *n*, which relates to the dimensionality of crystal growth, is 4 for the Avrami and 3 for the Gualtieri model. These values imply that for both the standard and humidified conditions the MOF crystallites grow in three dimensions, which might indicate the mobility of the ZIF-8 building blocks at the crystallization front. The Gualtieri b-value of ≤ 15 suggests that nucleation in both conditions is heterogeneous[45], as would be expected for a solvent-free process. The Gualtieri growth rate k_g increases approximately 20-fold under humidified conditions, to the range previously found for ZIF-8 formation in solution[53]. Water facilitates the oxide-to-MOF conversion through the direct hydroxylation of ZnO[33,54] as well as through the protonation of HmIM, which subsequently reacts with ZnO[55]. Furthermore, water vapor enhances the mobility of MOF building blocks as also observed in other preparation routes in the absence of bulk solvents[56,57]. When a MOF-CVD ZIF-8 film without unreacted ZnO precursor was exposed a second time to HmIM in the presence of water vapor, the film roughness increased through recrystallization (**Supplementary Figure 20**), in line with

previous observations[58]. In contrast, no recrystallization occurred when HmIM was introduced in the absence of moisture.

The oxide-to-MOF transformations discussed so far started from a 3 nm ALD ZnO layer. These thin precursor layers fully convert to a ~ 30 nm ZIF-8 layer, as evidenced by a constant optical thickness and weight at the end of the vapor-solid reaction (**Fig. 2a**, **Supplementary Fig. 7**), a steady mIM ToF-SIMS signal throughout the film (**Fig. 3b**), elemental profiles measured with ToF-ERDA (**Supplementary Fig. 21**), and specific surface area in agreement with a fully-formed MOF layer (**Fig. 3f**). For a 15 nm ZnO layer, *in situ* ellipsometry profile shows that initially, a ZIF-8 layer of a comparable thickness (~ 35 nm) is formed (**Fig. 4c, Supplementary Fig. 22**). However, a second, more pronounced thickness expansion is observed after longer HmIM exposure time, corresponding to the reaction of the ZnO precursor underneath the initially formed ZIF-8 layer. Likely, the initially formed ZIF-8 layer slows down the accumulation of a critical HmIM concentration in the remaining ZnO precursor layer, acting as an additional mass transfer resistance layer, thus delaying further nucleation. This MOF layer also prevents the water formed by the reaction of ZnO and HmIM from rapidly escaping, leading to crystallization conditions similar to a humidified environment and resulting in rough ZIF-8 films (R_{RMS} = 38.4 nm).

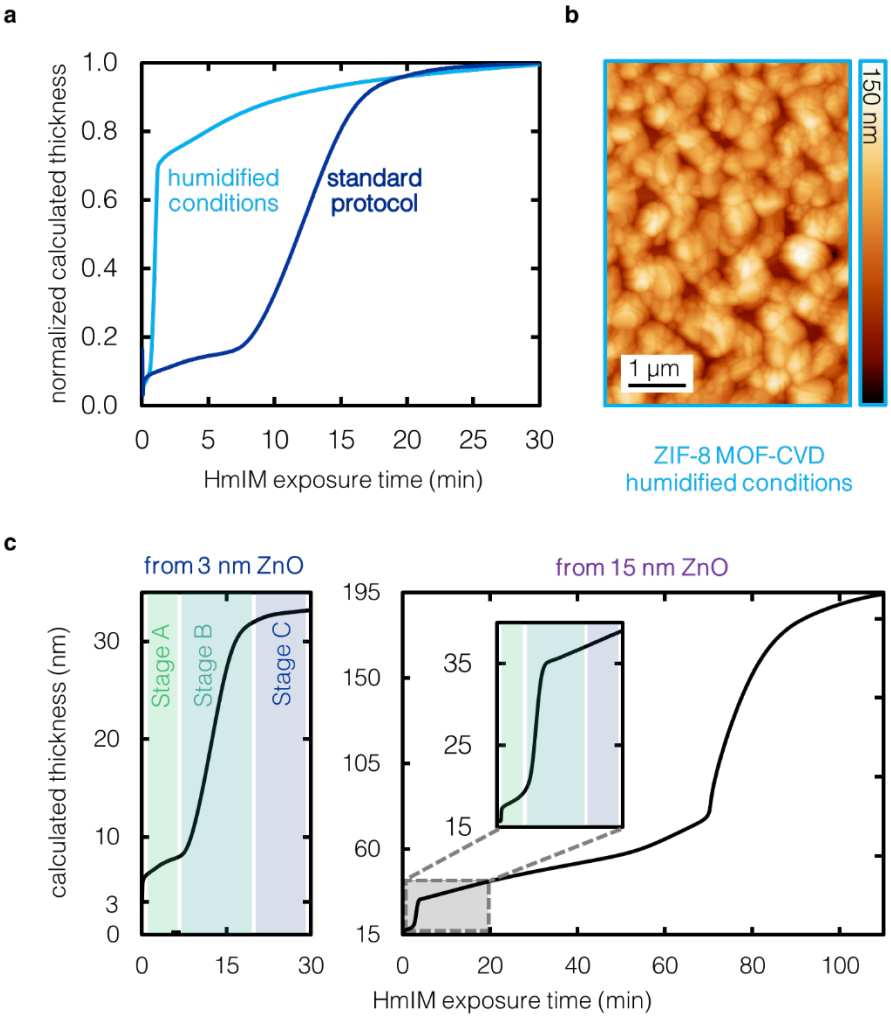

Figure 4 | Influence of humidity and ZnO precursor thickness. a, ZIF-8 MOF-CVD process from 3 nm ZnO, as a function of HmIM exposure time for the standard (dark blue) and humidified (light blue) conditions. **b,** AFM image of the film deposited under humidified conditions (R_{RMS} = 21 nm). **c,** *In situ* ellipsometry data collected during the conversion of 3 nm and 15 nm ALD ZnO.

Full wafer MOF-CVD

The impact of process temperature, oxide precursor thickness and ligand exposure time can be represented in a MOF-CVD process chart (**Fig. 5a, Supplementary Fig. 23-24**). For a specified thermal gradient, a minimum oxide precursor thickness is required to yield high-quality films. Furthermore, an optimal HmIM exposure time is needed to ensure complete ZnO conversion, yet avoid crystallite ripening. To show that these optimized deposition conditions for ZIF-8 can be translated to large substrates, experiments were performed on full 200 mm Si wafers. Aided by reactor simulations, we observed that a diffuser ring at the inlet of the MOF-CVD reactor chamber improves the exposure dynamics, resulting in a more uniform flow pattern and film deposition (**Supplementary Fig. 25**). The resulting transparent, mirror-like MOF coating has an average optical thickness of 31 ± 3.5 nm, as determined from a 100-point ellipsometry thickness mapping measurement (**Fig. 5b**). Using the wafer as a back electrode, conductive AFM measurements were performed at different positions to check for pinholes in the film. Scans at a bias of 8.0 V (**Fig. 5c**) confirm that the insulating MOF layer is pinhole-free at the nanoscale. As a negative control, the experiment was repeated for a MOF-CVD ZIF-8 sample deposited under humidified conditions. For this film, the pinholes that appear in between the crystallites as a result of ripening are clearly observed. Additionally, the pinhole-free nature of the optimized MOF-CVD ZIF-8 films was also confirmed on the millimeter scale using liquid metal top-contacts (**Supplementary Fig. 26**).

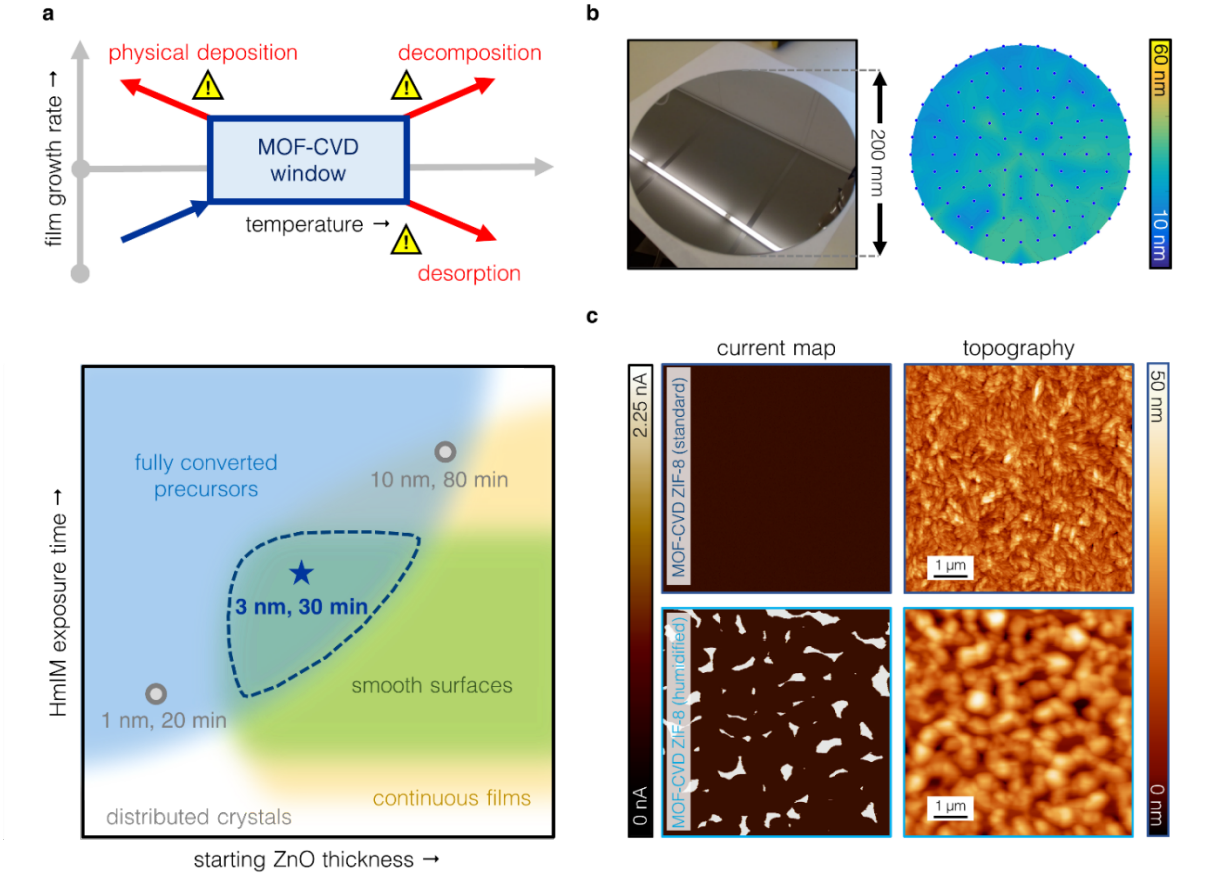

Figure 5 | Full-wafer ZIF-8 MOF-CVD. **a,** MOF-CVD process chart for ZIF-8 that shows the impact of temperature**,** ZnO precursor thickness and HmIM exposure time. **b,** Photograph of a full 200 mm wafer with MOF-CVD ZIF-8 coating and the corresponding ellipsometry thickness mapping. **c,** Current and topography maps obtained by conductive AFM for MOF-CVD ZIF-8 films deposited under standard (top) and humidified conditions (bottom). The regions where current is detected correspond to pinholes in the layer.

In summary, we demonstrated for the first time the scale-up of the MOF-CVD process in a fully integrated reactor compatible with cleanroom standards. Through *in situ* and *ex situ* techniques, the critical deposition parameters were identified for the case of ZIF-8 and the growth mechanism was elucidated. The optimized deposition conditions were successfully transferred to large-area substrates and characterized using the tools common in a cleanroom fabrication setting. The implementation of MOF-CVD as a standardized operation represents an important step in making this technique accessible to researchers from other fields and thus realize applications across traditional subject boundaries, especially in microelectronics.

Methods

Substrates. Device grade, p-type, single-side polished, back-etched 200 mm Si wafers (Si-Mat, resistivity = 1-30 $\Omega \cdot cm^{-1}$, thickness = 381 ± 25 µm) were used. Smaller pieces were cleaved and deposited with thin layers of Pt or Au as required for specific characterization techniques. Arrays of Si micropillars with a diameter and height of 2 and 50 µm, respectively, were produced by deep reactive ion etching (Bosch process). The pillars were separated 2 µm apart in a triangular-pitch geometry and were patterned by standard photolithography procedures using 600 nm SiO_2 as a hard mask.

ZIF-8 MOF-CVD

- **Step 1 - ALD ZnO. The** ZnO films were deposited using a modified Savannah S-200 thermal ALD reactor (Veeco Instruments, Inc.) with deionized water (DIW) and diethylzinc (DEZ, 97 %, STREM) as precursors. Nitrogen (99.999 %) was the carrier and purging gas used, sourced from a header line in the cleanroom facility. The pulse and purge durations for the ALD precursors were set to 0.015 s and 5 s, respectively. The reactor base pressure was ~ 0.40 mbar at an N_2 gas flow of 20 sccm. This process resulted in a ZnO growth rate of 1 $Å \cdot cycle^{-1}$ on Si substrates (**Supplementary Fig. 27**).

- **Step 2a - HmIM delivery step *standard protocol (non-humidified conditions)*. Start-up operation.** Three heating zones were used as a preventive measure for HmIM condensation along the reactor lines. The bubbler-type sublimation vessel, initially supplied with 30 g of freshly-ground HmIM (99 %, Sigma Aldrich), was set to 125 ºC, while the outlet and supply lines of the bubbler and the connections to the MOF CVD reactor were fixed to 130 ºC and 135 ºC, respectively. These lines were progressively heated in 30-minute intervals to prevent clogging during start-up. Before the depositions, purging and drying sequences (100 ºC, 30 min) were implemented to ensure the removal of air and moisture in the headspace of the bottle and the HmIM powder bed. **HmIM delivery.** The N_2 flow was stopped and the outlet valve was closed to ensure controlled HmIM delivery and saturation (stopped-flow conditions) inside the reactor with an N_2 bubbler pressure of 110 mbar.

- **Activation protocol.** The recipe was terminated with an evacuation step and with the N_2 flow maintained at 20 sccm. The dynamic vacuum was kept as the substrate temperature was ramped up and held briefly at 150 ºC until a constant profile is recorded with *in situ* ellipsometry (~ 10 minutes). The activation protocol was implemented for all depositions in this work unless otherwise specified.

- **Step 2b - HmIM delivery step *humidified conditions*.** Immediately before dosing HmIM (described above as Step 2a), water was introduced by means of pulses, achieving ~ 12 % relative humidity in the reactor. This value was estimated by noting the pressure increase in the reactor after dosing, divided by the water saturation pressure at the substrate temperature (80 ºC).

- **Precursor aging:** a delay in nucleation occurs after prolonged use of the same HmIM batch (**Supplementary Fig. 28-29**), likely because of slower sublimation kinetics because of HmIM particle growth (**Supplementary Fig. 30-31**). This occurrence is a

consideration for process scale-up, to ensure a surface-saturating and sustained vapor flux. Industrial solutions exist for handling this difficulty for solid precursors, including fluidization[59] and solvent-assisted delivery[60].

***In situ* and *ex situ* ellipsometry.** The optical properties of the deposited layers were measured using an M-2000x spectroscopic ellipsometer (J. A. Woollam Co. Inc., λ = 246-1000 nm). For *in situ* measurements, a custom reactor lid with fused silica viewports was used to collect ellipsometry information (Psi and Delta). The raw ellipsometry data were fitted using various methods (**Supplementary Section II**). **Full wafer thickness mapping.** The thickness and refractive index (λ = 633 nm) of the ZIF-8 layers deposited on 200 mm wafers were measured with a KLA-Tencor ASET F5x thin film measurement system equipped with a motorized stage. A radial map of Psi and Delta (λ = 400-800 nm) was recorded for 100 points evenly distributed over the wafer and processed using the appropriate optical model. **Methanol ellipsometric porosimetry.** The samples were placed inside a custom porosimetry chamber equipped with an ellipsometer (Sentech SE801, λ = 350 - 850 nm) and a programmable adsorbate dosing platform. Data were recorded at room temperature, with an equilibration time of 30 s for each data point.

QCM monitoring. The change in mass of the deposited film was monitored via a QCM setup integrated into the reactor lid. Au-coated AT-cut quartz crystals (Inficon, fundamental frequency ~6 MHz) were used. Frequencies (590 data points per second) were recorded using an Inficon STM2 QCM monitoring system. The Sauerbrey equation was employed to estimate the mass increase from the change in frequency[61]. The in-house developed thermal insulation cover resulted in a QCM stabilization time of approximately 1 hour, which was respected for all experiments.

Atomic Force Microscopy (AFM). AFM Imaging. Topography images (6 μm × 6 μm and 2 μm × 2 μm, 1024 × 1024 pixels) were recorded in intermittent contact mode with a PicoSPM

(5500, Agilent Technologies) setup in ambient conditions using Si cantilevers (AC160TS-R3). Data analysis was performed using WSXM 5.0 software[62]. **Conductive AFM.** A Bruker's Dimension Icon AFM system was used to check for pinholes in films deposited under standard and humidified conditions on Si substrates. The samples were electrically contacted with Ag paint using a custom sample holder. A heavily doped full diamond tip was used to test the samples with an applied DC bias voltage of 8.0 V at a scan speed of 0.5 Hz. The threshold bias voltage for the standard MOF-CVD ZIF-8 coating was determined to be > 5.0 V. All measurements were carried out in a glove box under an Ar atmosphere.

X-ray characterization. Measurements were performed on a Malvern PANalytical Empyrean diffractometer equipped with a PIXcel3D solid-state detector using a Cu anode. Before each measurement, an iterative scheme was employed to optimize both sample height and tilt. **X-ray reflectivity.** Data were collected between incident angles of -0.03 º and 4.5 º with a step size of 0.005 º and a counting time of 8.8 s. **Grazing incidence-XRD.** Diffraction patterns were recorded in reflection geometry (incident beam angle 0.02 °) within a 5 ° - 45 ° 2θ range, using a step size of 0.053 ° and a counting time of 1000 s per step. On the incident beam side, a 1/16° fixed anti-scatter slit was used to limit the divergence of the beam. **Synchrotron GI-XRD**. The measurements were conducted at the ID10-EH beamline of European Synchrotron Radiation Facility (ERSF) in Grenoble, France, with a beam energy of 8 keV and a grazing angle of 0.19 °. The collected two-dimensional data were processed using GIDVis[63]

Ion beam analysis. Time-of-flight Elastic Recoil Detection (ToF-ERD). A 6SDH Pelletron particle accelerator (National Electrostatics Corporation) equipped with an 8.0 MeV $^{35}Cl^{4+}$ primary ion beam was used. The areal density (atoms·cm^{-2}) and elemental composition of the ALD ZnO coating on Si substrates were measured at a scattering angle and sample tilt of 40.5 ° and 10 °, respectively. The same recoil signals were considered for all elements except for Zn, where the scattered Cl signal was used. After instrument calibration, the effect of elemental

losses resulting from interactions between the sample and the ion beam was considered negligible. **Rutherford Back Scattering (RBS)** was used to determine the metal density of the oxide precursor using a He-beam with an energy of 1.523 MeV and a beam current of 45 nA. The scattering and tilt angles were set to 170 ° and 11 °, respectively.

X-ray Photoelectron Spectroscopy (XPS). XPS data for the ALD ZnO and MOF-CVD ZIF-8 films were collected using a PHI5600 Versaprobe II (Physical Electronics) utilizing a Al Kα monochromatic X-ray source (1486.71 eV photon energy) with a beam irradiation power of 25 W. The kinetic energy of the photoelectrons was measured with a take-off angle of 45° and with a spot diameter of 100 μm to measure surface compositions up to ~10 nm in depth. The vacuum in the analysis chamber was better than 1 x 10^{-9} Torr during measurements. Survey scans were recorded with a pass energy of 187.85 eV and an energy step size of 0.1 eV. After identification of the elements of interest using PHI Multipak software (v9.5), high-resolution scans of Zn 2p, C 1s, O 1s, and N 1s were obtained with a pass energy of 23.5 eV and with an energy step size of 0.05 eV. Dual-beam charge neutralization was used to compensate for potential charging effects. The analysis and fitting were performed using CasaXPS software (Casa Software, Ltd.) employing a mixed Gaussian-Lorentzian peak shape and a Shirley type background. The probe depths for the films was found to be 3-5 nm, calculated by multiplying the inelastic mean free path (IMFP) to three and to the cosine of the measurement angle for every electron energy of interest. The IMFP was evaluated using the Tanuma, Powel, and Penn (TPP-2M) relation[64].

Infrared spectroscopy. A Varian 670 FTIR spectrometer with a Ge crystal plate in the Veemax III module, operated on attenuated total reflection geometry was used. The IR spectra of the films deposited on Au-coated Si substrates was obtained using the actively cooled mercury cadmium telluride detector.

Time-of-flight secondary ion mass spectroscopy (ToF-SIMS). The samples at different MOF-CVD growth stages were probed using a TOF-SIMS 5 instrument (ION-TOF GmbH). A 30 keV Bi_3^+ analysis beam was used in a high-current bunched mode for high mass resolution ($m \cdot \Delta m^{-1}$ ~ 8000 at 29 u, $^{29}Si^+$). The primary ion dose was kept sufficiently low so that the static limit of 1×10^{13} ions·cm^{-2} per analysis was not exceeded. The pressure in the chamber was better than 3.4×10^{-8} mbar during measurements. The accuracy of mass assignments, expressed as deviation (in ppm), is calculated by taking the difference between the experimental and theoretical mass of a fragment and dividing this number by the experimental mass. Deviations of ≤ 50 ppm are indicative of satisfactory assignments. Depth profiles were obtained in a dual beam configuration, where a 2.5 keV Ar_{1100}^+ cluster ion beam was used as a sputter beam and Bi_3^+ was used to analyze a 100 µm × 100 µm area at the bottom of the 250 µm × 250 µm crater.

Krypton physisorption. Using a Micromeritics 3Flex 3500 instrument, sorption measurements on the coatings have been performed as described in our previous work[10].

Electron microscopy. Images were collected using a Philips XL30 FEG. Prior to imaging, the samples were coated with 5 nm of Pt.

Optical microscopy. An S lynx compact profilometer (Sensofar) was used to image HmIM particles. The images were acquired using a Nikon TU Plan Fluor lens with a magnification of 10× and 20× and subsequently processed using SensoSCAN.

Electrical characterization. A drop of a eutectic mixture of gallium and indium (EGaIn, 99.99 %, Alfa Aesar) was used as the top electrical contact on MOF-CVD ZIF-8 films deposited on Pt-coated Si substrates. Current (I) was measured as a function of the applied bias (V) with the Pt bottom electrode contacted with Ag paint. At least 10 I-V curves were acquired at 5-10 different positions on the sample using a Yokogawa GS200 and a Keithley 6517B/2400 as the

voltage source and ammeter, respectively. The contact areas, ranging from 100×10^{-6} to 400×10^{-6} cm^2, were estimated using a CCD camera. All instruments were controlled using custom software. The generated current density (J) histograms were fitted using Gaussian functions for determining the peak center and width.

Data availability. Data supporting the findings of this study are available from the corresponding author upon request.

Acknowledgments

This project has received funding from the European Research Council (ERC) under the European Union's Horizon 2020 research and innovation program (grant agreement n° 716472, acronym: VAPORE). The Research Foundation-Flanders (FWO) is acknowledged for funding in the research projects G083016N, 1529618N, ZW13_07 (Hercules Program), 1501618N, and the infrastructure project G0H0716N. I.S., T.H., and T.S. thank FWO for the fellowships 12L5417N, 1295317N, and 1S53318N, respectively. V.R-G. is grateful for the doctoral fellowship (FPU13/03203) awarded by the Spanish Ministry of Education, Culture, and Sports. A.J.C. acknowledges Silvia Armini, Jill Serron, Lennaert Wouters, Praveen Dara, and Oliver Feddersen-Clausen for scientific support. The authors acknowledge the European Synchrotron Radiation Facility (ESRF) for the provision of synchrotron radiation facilities and would like to thank Oleg Konovalov and Andrey Chumakov for the assistance in using beamline ID10-EH for GI-XRD experiments. A.J.C., T.S., and S.R. are grateful to Roland Resel's group (TU Graz, Austria) for guidance in the data processing. Insights stemming from discussions with researchers in the field were enabled through COST Action MP1402 - Hooking together European research in Atomic Layer Deposition (HERALD), supported by COST (European Cooperation in Science and Technology).

Contributions

A.J.C., I.S., and R.A. conceived and designed the experiments. A.J.C. carried out and analyzed all depositions and a majority of the sample characterization. A.J.C. and I.S. implemented the MOF-CVD process in the automated reactor and developed the *in situ* monitoring protocols. M.K., T.S., S.R-H., S.P., P.V., J.T., S.D.F., C.M-G. and T.H. provided support in the analyses of results. A.J.C. and S.P. carried out XPS measurements and data analysis. K.M. and A.J.C. performed the ToF-SIMS measurements. V.R-G. and S.T. carried out the electrical characterization. The manuscript was written by A.J.C. under the guidance of I.S. and R.A., with input from all authors. Correspondence and requests for materials should be addressed to R.A.

Competing financial interests

The authors declare no competing financial interests.

References

1. Yang, D. & Gates, B. C. Catalysis by Metal Organic Frameworks: Perspective and Suggestions for Future Research. *ACS Catal.* **9**, 1779–1798 (2019).
2. Ma, S. & Zhou, H.-C. Gas storage in porous metal–organic frameworks for clean energy applications. *Chem Commun* **46**, 44–53 (2010).
3. Kwon, H. T., Jeong, H.-K., Lee, A. S., An, H. S. & Lee, J. S. Heteroepitaxially Grown Zeolitic Imidazolate Framework Membranes with Unprecedented Propylene/Propane Separation Performances. *J. Am. Chem. Soc.* **137**, 12304–12311 (2015).
4. Stassen, I. *et al.* An updated roadmap for the integration of metal–organic frameworks with electronic devices and chemical sensors. *Chem Soc Rev* **46**, 3185–3241 (2017).
5. Allendorf, M. D., Schwartzberg, A., Stavila, V. & Talin, A. A. A Roadmap to Implementing Metal–Organic Frameworks in Electronic Devices: Challenges and Critical Directions. *Chem. – Eur. J.* **17**, 11372–11388 (2011).
6. Wang, H., Lustig, W. P. & Li, J. Sensing and capture of toxic and hazardous gases and vapors by

metal–organic frameworks. *Chem. Soc. Rev.* **47**, 4729–4756 (2018).

7. Yassine, O. *et al.* H $_2$ S Sensors: Fumarate-Based fcu-MOF Thin Film Grown on a Capacitive Interdigitated Electrode. *Angew. Chem. Int. Ed.* **55**, 15879–15883 (2016).
8. Stassen, I. *et al.* Towards metal–organic framework based field effect chemical sensors: UiO-66-NH $_2$ for nerve agent detection. *Chem Sci* **7**, 5827–5832 (2016).
9. Eslava, S. *et al.* Metal-Organic Framework ZIF-8 Films As Low-κ Dielectrics in Microelectronics. *Chem. Mater.* **25**, 27–33 (2013).
10. Stassen, I. *et al.* Chemical vapour deposition of zeolitic imidazolate framework thin films. *Nat. Mater.* **15**, 304–310 (2016).
11. Lew, C. M., Cai, R. & Yan, Y. Zeolite Thin Films: From Computer Chips to Space Stations. *Acc. Chem. Res.* **43**, 210–219 (2010).
12. Ozaydin-Ince, G., Coclite, A. M. & Gleason, K. K. CVD of polymeric thin films: applications in sensors, biotechnology, microelectronics/organic electronics, microfluidics, MEMS, composites and membranes. *Rep. Prog. Phys.* **75**, 016501 (2012).
13. Ahvenniemi, E. & Karppinen, M. Atomic/molecular layer deposition: a direct gas-phase route to crystalline metal–organic framework thin films. *Chem. Commun.* **52**, 1139–1142 (2016).
14. Ahvenniemi, E. & Karppinen, M. In Situ Atomic/Molecular Layer-by-Layer Deposition of Inorganic–Organic Coordination Network Thin Films from Gaseous Precursors. *Chem. Mater.* **28**, 6260–6265 (2016).
15. Tanskanen, A. & Karppinen, M. Iron-Terephthalate Coordination Network Thin Films Through In-Situ Atomic/Molecular Layer Deposition. *Sci. Rep.* **8**, 8976 (2018).
16. Medishetty, R. *et al.* Fabrication of zinc-dicarboxylate- and zinc-pyrazolate-carboxylate-framework thin films through vapour–solid deposition. *Dalton Trans.* **47**, 14179–14183 (2018).
17. Lausund, K. B. & Nilsen, O. All-gas-phase synthesis of UiO-66 through modulated atomic layer deposition. *Nat. Commun.* **7**, 13578 (2016).
18. Lausund, K. B., Petrovic, V. & Nilsen, O. All-gas-phase synthesis of amino-functionalized UiO-66 thin films. *Dalton Trans.* **46**, 16983–16992 (2017).
19. Salmi, L. D. *et al.* Studies on atomic layer deposition of MOF-5 thin films. *Microporous Mesoporous Mater.* **182**, 147–154 (2013).
20. Salmi, L. D. *et al.* Studies on atomic layer deposition of IRMOF-8 thin films. *J. Vac. Sci. Technol.*

A **33**, 01A121 (2014).

21. Tynell, T. & Karppinen, M. Atomic layer deposition of ZnO: a review. *Semicond. Sci. Technol.* **29**, 043001 (2014).

22. Park, K. S. *et al.* Exceptional chemical and thermal stability of zeolitic imidazolate frameworks. *Proc. Natl. Acad. Sci.* **103**, 10186–10191 (2006).

23. Li, W. *et al.* Ultrathin metal–organic framework membrane production by gel–vapour deposition. *Nat. Commun.* **8**, (2017).

24. Young, C. *et al.* Controlled Chemical Vapor Deposition for Synthesis of Nanowire Arrays of Metal–Organic Frameworks and Their Thermal Conversion to Carbon/Metal Oxide Hybrid Materials. *Chem. Mater.* **30**, 3379–3386 (2018).

25. Xu, P., Liu, M., Li, X., Xu, T. & Zhang, Y. Multi-dimensional multi-level sensing nanostructure for high-performance detection to trace-level dopamine molecules. in *2017 19th International Conference on Solid-State Sensors, Actuators and Microsystems (TRANSDUCERS)* 762–765 (2017).

26. Ma, X. *et al.* Zeolitic imidazolate framework membranes made by ligand-induced permselectivation. *Science* **361**, 1008–1011 (2018).

27. Jiménez, P., Roux, M. V. & Turrión, C. Thermochemical properties of N-heterocyclic compounds IV. Enthalpies of combustion, vapour pressures and enthalpies of sublimation, and enthalpies of formation of 2-methylimidazole and 2-ethylimidazole. *J. Chem. Thermodyn.* **24**, 1145–1149 (1992).

28. Coclite, A. M. *et al.* 25th Anniversary Article: CVD Polymers: A New Paradigm for Surface Modification and Device Fabrication. *Adv. Mater.* **25**, 5392–5423 (2013).

29. Gleason, K. K. *CVD Polymers: Fabrication of Organic Surfaces and Devices*. (John Wiley & Sons, 2015).

30. Rocklein, M. N. & George, S. M. Temperature-Induced Apparent Mass Changes Observed during Quartz Crystal Microbalance Measurements of Atomic Layer Deposition. *Anal. Chem.* **75**, 4975–4982 (2003).

31. Riha, S. C., Libera, J. A., Elam, J. W. & Martinson, A. B. F. Design and implementation of an integral wall-mounted quartz crystal microbalance for atomic layer deposition. *Rev. Sci. Instrum.* **83**, 094101 (2012).

32. Mackus, A. J. M., MacIsaac, C., Kim, W.-H. & Bent, S. F. Incomplete elimination of precursor ligands during atomic layer deposition of zinc-oxide, tin-oxide, and zinc-tin-oxide. *J. Chem. Phys.* **146**, 052802 (2016).

33. Weckman, T. & Laasonen, K. Atomic Layer Deposition of Zinc Oxide: Diethyl Zinc Reactions and Surface Saturation from First-Principles. *J. Phys. Chem. C* **120**, 21460–21471 (2016).

34. Ginley, D. S. *Handbook of Transparent Conductors*. (Springer Science & Business Media, 2010).

35. Stassen, I., De Vos, D. & Ameloot, R. Vapor-Phase Deposition and Modification of Metal-Organic Frameworks: State-of-the-Art and Future Directions. *Chem. - Eur. J.* **22**, 14452–14460 (2016).

36. Tao, J. *et al.* Hybrid Photonic Cavity with Metal-Organic Framework Coatings for the Ultra-Sensitive Detection of Volatile Organic Compounds with High Immunity to Humidity. *Sci. Rep.* **7**, 41640 (2017).

37. Esken, D. *et al.* ZnO@ZIF-8: stabilization of quantum confined ZnO nanoparticles by a zinc methylimidazolate framework and their surface structural characterization probed by CO2 adsorption. *J. Mater. Chem.* **21**, 5907 (2011).

38. Kalidindi, S. B., Esken, D. & Fischer, R. A. B□N Chemistry@ZIF-8: Dehydrocoupling of Dimethylamine Borane at Room Temperature by Size-Confinement Effects. *Chem. - Eur. J.* **17**, 6594–6597 (2011).

39. Tu, M. *et al.* Reversible Optical Writing and Data Storage in an Anthracene-Loaded Metal–Organic Framework. *Angew. Chem.* **131**, 2445–2449 (2019).

40. Campagnol, N., Stassen, I., Binnemans, K., de Vos, D. E. & Fransaer, J. Metal–organic framework deposition on dealloyed substrates. *J. Mater. Chem. A* **3**, 19747–19753 (2015).

41. Zhang, K. *et al.* Alcohol and water adsorption in zeolitic imidazolate frameworks. *Chem. Commun.* **49**, 3245–3247 (2013).

42. Avrami, M. Kinetics of Phase Change. II Transformation-Time Relations for Random Distribution of Nuclei. *J. Chem. Phys.* **8**, 212–224 (1940).

43. Avrami, M. Kinetics of Phase Change. I General Theory. *J. Chem. Phys.* **7**, 1103–1112 (1939).

44. Avrami, M. Granulation, Phase Change, and Microstructure Kinetics of Phase Change. III. *J. Chem. Phys.* **9**, 177–184 (1941).

45. Gualtieri, A. F. Synthesis of sodium zeolites from a natural halloysite. *Phys. Chem. Miner.* **28**, 719–728 (2001).

46. Bueken, B. *et al.* An in situ investigation of the water-induced phase transformation of UTSA-74 to MOF-74(Zn). *CrystEngComm* **19**, 4152–4156 (2017).

47. Patterson, J. P. *et al.* Observing the Growth of Metal–Organic Frameworks by *in Situ* Liquid Cell Transmission Electron Microscopy. *J. Am. Chem. Soc.* **137**, 7322–7328 (2015).

48. Osta, R. E., Feyand, M., Stock, N., Millange, F. & Walton, R. I. Crystallisation Kinetics of Metal Organic Frameworks From in situ Time-Resolved X-ray Diffraction. *Powder Diffr.* **28**, S256–S275 (2013).

49. Ahnfeldt, T. *et al.* High-Throughput and Time-Resolved Energy-Dispersive X-Ray Diffraction (EDXRD) Study of the Formation of CAU-1-(OH)2: Microwave and Conventional Heating. *Chem. – Eur. J.* **17**, 6462–6468 (2011).

50. Millange, F. *et al.* Time-Resolved In Situ Diffraction Study of the Solvothermal Crystallization of Some Prototypical Metal–Organic Frameworks. *Angew. Chem. Int. Ed.* **49**, 763–766 (2010).

51. Jeong, T. H., Kim, M. R., Seo, H., Kim, S. J. & Kim, S. Y. Crystallization behavior of sputter-deposited amorphous Ge2Sb2Te5 thin films. *J. Appl. Phys.* **86**, 774–778 (1999).

52. Bass, J. D., Grosso, D., Boissiere, C. & Sanchez, C. Pyrolysis, Crystallization, and Sintering of Mesostructured Titania Thin Films Assessed by in Situ Thermal Ellipsometry. *J. Am. Chem. Soc.* **130**, 7882–7897 (2008).

53. Yeung, H. H.-M. *et al.* Control of Metal–Organic Framework Crystallization by Metastable Intermediate Pre-equilibrium Species. *Angew. Chem. Int. Ed.* **58**, 566–571 (2019).

54. Newberg, J. T. *et al.* ZnO($10\bar{1}0$) Surface Hydroxylation under Ambient Water Vapor. *J. Phys. Chem. B* **122**, 472–478 (2018).

55. Cliffe, M. J., Mottillo, C., Stein, R. S., Bučar, D.-K. & Friščić, T. Accelerated aging: a low energy, solvent-free alternative to solvothermal and mechanochemical synthesis of metal–organic materials. *Chem. Sci.* **3**, 2495–2500 (2012).

56. Shi, Q., Chen, Z., Song, Z., Li, J. & Dong, J. Synthesis of ZIF-8 and ZIF-67 by Steam-Assisted Conversion and an Investigation of Their Tribological Behaviors. *Angew. Chem. Int. Ed.* **50**, 672–675 (2011).

57. Mottillo, C. *et al.* Mineral neogenesis as an inspiration for mild, solvent-free synthesis of bulk

microporous metal–organic frameworks from metal (Zn, Co) oxides. *Green Chem.* **15**, 2121–2131 (2013).

58. Taek Kwon, H. *et al.* Defect-induced ripening of zeolitic-imidazolate framework ZIF-8 and its implication to vapor-phase membrane synthesis. *Chem. Commun.* **52**, 11669–11672 (2016).

59. Vahlas, C. *et al.* A Delivery System for Precursor Vapors Based on Sublimation in a Fluidized Bed. *Chem. Vap. Depos.* **13**, 123–129 (2007).

60. Vahlas, C., Caussat, B., Gladfelter, W., Senocq, F. & Gladfelter, E. Liquid and Solid Precursor Delivery Systems in Gas Phase Processes. *Recent Pat. Mater. Sci.* **8**, 91–108 (2015).

61. Sauerbrey, G. Verwendung von Schwingquarzen zur Wägung dünner Schichten und zur Mikrowägung. *Z. Für Phys.* **155**, 206–222 (1959).

62. Horcas, I. *et al.* WSXM: A software for scanning probe microscopy and a tool for nanotechnology. *Rev. Sci. Instrum.* **78**, 013705 (2007).

63. GIDVis – About. Available at: http://www.if.tugraz.at/amd/GIDVis/About.html. (Accessed: 8th September 2018)

64. Tanuma, S., Powell, C. J. & Penn, D. R. Calculation of electron inelastic mean free paths (IMFPs) VII. Reliability of the TPP-2M IMFP predictive equation. *Surf. Interface Anal.* **35**, 268–275 (2003).